Fermi surface anisotropy in plasmonic metals increases the potential for efficient hot carrier extraction

Sushant Kumar [1], Christian Multunas [2], and Ravishankar Sundararaman [1,2,*]

[1]*Department of Materials Science & Engineering, Rensselaer Polytechnic Institute, 110 8th Street, Troy, New York 12180, USA*
[2]*Department of Physics, Applied Physics, and Astronomy, Rensselaer Polytechnic Institute, 110 8th Street, Troy, New York 12180, USA*

Realizing the potential of plasmonic hot carrier harvesting for energy conversion and photodetection requires new materials that resolve the bottleneck of extracting carriers prior to energy relaxation within the metal. Using first-principles calculations of optical response and carrier transport properties, we show that directional conductors with Fermi velocities restricted predominantly to one or two directions present significant advantages for efficient hot carrier harvesting. We show that the optical response of filmlike conductors $PtCoO_2$ and Cr_2AlC resembles that of two-dimensional (2D) metals, while that of wirelike conductors CoSn and YCo_3B_2 resembles that of 1D metals, which can lead to high mode confinement and efficient light collection in small dimensions, while still working with 3D materials with high carrier densities. Carrier lifetimes and transport distances in these materials, especially in $PtCoO_2$ and CoSn, are competitive with noble metals. Most importantly, we predict that the carrier injection efficiency from all of these materials into semiconductors can exceed 10% due to the small component of carrier momentum parallel to the metal surface, substantially improving upon the typical injection efficiency of less than 0.1% from noble metals into semiconductors.

I. INTRODUCTION

High-energy electrons and holes excited in metal nanostructures upon the decay of plasmons provide a pathway to leverage light collected efficiently at the nanoscale for photochemistry [1], imaging [2], and photovoltaic energy conversion [3]. A continuing challenge in plasmonic hot carrier applications is utilizing the excited carriers prior to energy relaxation in the metal [4,5], requiring nanostructures smaller than the mean free paths of carriers and material interfaces that are capable of extracting a large fraction of carriers from the metal [6].

The field of plasmonic hot carriers has made great strides in expanding the space of materials from noble metals to include refractory plasmonic materials [7] such as transition metal nitrides [8–10] and low-dimensional materials such as MXenes [11–13]. These materials remain stable at smaller dimensions than noble metals, making it possible to minimize energy losses during the transport of carriers across the nanostructure [10]. Additionally, lower-dimensional plasmonic materials can exhibit higher mode confinement than three-dimensional (3D) metals, allowing efficient light capture at smaller length scales [14]. However, the overall efficiency of extracting hot carriers from plasmonic metals into semiconductors for photovoltaic and photodetection applications remains low, primarily due to the mismatch between carrier momenta near the Fermi energy in metals and the band edges in semiconductors [15–17], requiring further advances in materials for plasmonic hot carriers [6].

Here, we propose that directional conductors—three-dimensional materials that behave like lower-dimensional metals due to Fermi velocities restricted to one or two dimensions—have the potential to simultaneously absorb light efficiently at nanoscale dimensions and inject carriers with high probability into semiconductors. These directional conductors typically have highly anisotropic crystal structures (e.g., layered materials) which lead to highly anisotropic Fermi surfaces with directional properties. Using first-principles calculations of electronic structure, optical response, electron-phonon and electron-electron scattering, we show that the best directional conductors, including $PtCoO_2$ and CoSn, are competitive with noble metals in their frequency range of plasmonic response and carrier transport distances. We show that their optical response resembles lower-dimensional metals, which may allow the design of plasmonic nanostructures with more efficient light collection at small dimensions than their 3D counterparts. Finally, we show that the lower magnitude of Fermi momenta and the strong directional distribution can be leveraged to greatly enhance the probability of carrier injection into the semiconductor: from below 0.1% typical for noble metals to over 10% for the directional conductors as predicted by a modified Fowler model.

II. METHODS

A. Computational details

We perform electronic structure calculations using the open-source JDFTX software for density-functional theory (DFT) in the plane-wave basis [18]. We use the Perdew-Burke-Ernzerhof generalized gradient approximation to the exchange correlation functional [19], with nonrelativistic

*sundar@rpi.edu

125201-1

TABLE I. Number of atoms per unit cell N_{atoms} and converged lattice parameters for each material. The experimental lattice parameters a and c for $PtCoO_2$ [21], Cr_2AlC [22], CoSn [23], and YCo_3B_2 [24] are provided in parentheses for comparison next to the DFT-predicted values.

Material	N_{atoms}	a (Å)	c (Å)
$PtCoO_2$	12	2.85 (2.82)	18.03 (17.81)
Cr_2AlC	8	2.85 (2.86)	12.75 (12.82)
CoSn	6	5.26 (5.28)	4.26 (4.26)
YCo_3B_2	6	5.00 (5.04)	3.04 (3.03)

ultrasoft Garrity-Bennett-Rabe-Vanderbilt (GBRV) pseudopotentials at kinetic energy cutoffs of 20 hartrees for the wave functions and 100 hartrees for the charge density [20]. We optimize lattice parameters and internal geometries self-consistently for each material and calculate phonons and electron-phonon coupling from first principles. The converged lattice parameters have been compared with the corresponding experimental measurements in Table I. We use a k mesh of $12 \times 12 \times 2$ for $PtCoO_2$ and $12 \times 12 \times 12$ for Cr_2AlC, CoSn, and YCo_3B_2. For our phonon calculations, we use a q-point sampling of $3 \times 3 \times 1$ for $PtCoO_2$, $3 \times 3 \times 2$ for Cr_2AlC, and $3 \times 3 \times 3$ for CoSn and YCo_3B_2.

We construct maximally localized Wannier functions for each material to accurately reproduce the electronic band structure up to at least 40 eV above the Fermi level and use them to transform electron and phonon properties using the Wannier module of JDFTX [18,25]. For each of these materials, we use a combination of atomic orbitals and Gaussian orbitals ($\sigma = 1$ bohr) as the initial guesses or trial orbitals. The Gaussian orbitals are centered at random positions inside the unit cell. We use 5 d orbitals per Pt and Co atom, 1 s orbital and 3 p orbitals per O atom, and 105 Gaussian orbitals for $PtCoO_2$ (159 in total). For Cr_2AlC, we use 103 Gaussian orbitals. We use 5 d orbitals per Co atom, 5 d orbitals and 3 p orbitals per Sn atom, and 100 Gaussian orbitals for the case of CoSn (139 in total). Lastly, for YCo_3B_2 we use 5 d orbitals per Co atom, 5 d orbitals and 3 p orbitals per Y atom, 1 s orbital and 3 p orbitals per B atom, and 90 Gaussian orbitals (121 in total). Figure S3 in the Supplemental Material [26] shows that the real-space representations of the electronic Hamiltonian, dynamical matrix, and electron-phonon matrix elements all decay rapidly with distance [27], falling to 10^{-5}–10^{-6} of their maximum values by the edge of the corresponding supercells.

Using these, we interpolate electronic energies $\varepsilon_{\mathbf{k}n}$ at wave vector $\mathbf{k}$ and band n, their band velocities $v_{\mathbf{k}n}$ and velocity matrix elements $v_{\mathbf{k}n'n}$, phonon frequencies $\omega_{\mathbf{q}\alpha}$ at wave vector $\mathbf{q}$ and polarization α, and the electron-phonon matrix elements $g_{\mathbf{k}'n',\mathbf{k}n}^{\mathbf{k}'-\mathbf{k},\alpha}$ to significantly finer $\mathbf{k}$ and $\mathbf{q}$ meshes for integrals over the Brillouin zone (BZ) in the calculation of optical and carrier transport properties described next [28].

B. Dielectric functions

We calculate the complex dielectric tensor,

$$\bar{\epsilon}(\omega) = 1 + \frac{4\pi i (\bar{\sigma}_0/\tau_{D0})}{\omega(\tau_D^{-1}(\omega) - i\omega)} + \bar{\epsilon}_d(\omega), \quad (1)$$

where $\bar{\sigma}_0$ and τ_{D0} are the frequency-independent (static) conductivity tensor and Drude lifetime, respectively, and τ_D is the frequency-dependent momentum relaxation time. The second term captures the Drude response including the effect of phonon-assisted intraband transitions, while the final term, $\bar{\epsilon}_d(\omega)$, captures the effect of direct optical transitions. We evaluate the final term directly using Fermi's golden rule for the real part [29],

$$\text{Im } \bar{\epsilon}_d(\omega) = \frac{4\pi^2 e^2}{\omega^2} \int_{\text{BZ}} \frac{g_s\, d\mathbf{k}}{(2\pi)^3} \sum_{n'n} (f_{\mathbf{k}n} - f_{\mathbf{k}n'})$$
$$\times \delta(\varepsilon_{\mathbf{k}n'} - \varepsilon_{\mathbf{k}n} - \hbar\omega)(\mathbf{v}_{\mathbf{k}n'n}^* \otimes \mathbf{v}_{\mathbf{k}n'n}), \quad (2)$$

where $g_s = 2$ is the spin degeneracy factor and $f_{\mathbf{k}n}$ are the Fermi occupations of each electronic state. We then evaluate $\text{Re } \bar{\epsilon}_d(\omega)$ from it using the Kramers-Kronig relation. The energy-conserving δ function above is broadened to a Lorentzian due to electron-electron and electron-phonon scattering linewidths, which we also calculate from first principles as described below in Sec. II C [28].

In the Drude term above [second term of (1)], we account for phonon-assisted transitions within the frequency-dependent momentum relaxation rate,

$$\tau_D^{-1}(\omega) = \frac{2\pi}{\hbar g(\varepsilon_F) b_T(\hbar\omega)} \sum_{\alpha\pm} \int_{\text{BZ}} \frac{d\mathbf{q}}{(2\pi)^d}$$
$$\times G_{\mathbf{q}\alpha}^p \frac{\pm b_T(\hbar\omega \pm \hbar\omega_{\mathbf{q}\alpha})}{e^{\pm\hbar\omega_{\mathbf{q}\alpha}/k_BT} - 1}, \quad (3)$$

derived from the Eliashberg spectral function [30] and generalized to nonzero temperature [14]. Here, $g(\varepsilon_F)$ is the density of electronic states at the Fermi level, $b_T(\varepsilon) \equiv \varepsilon/(1 - e^{-\varepsilon/k_BT})$ and

$$G_{\mathbf{q}\alpha}^p \equiv \sum_{nn'} \int_{\text{BZ}} \frac{g_s\Omega\, d\mathbf{k}}{(2\pi)^d} \left|g_{(\mathbf{k}+\mathbf{q})n',\mathbf{k}n}^{\mathbf{q}\alpha}\right|^2 \delta(\varepsilon_{\mathbf{k}n} - \varepsilon_F)$$
$$\times \delta(\varepsilon_{(\mathbf{k}+\mathbf{q})n'} - \varepsilon_F) \left(1 - \frac{\mathbf{v}_{\mathbf{k}n} \cdot \mathbf{v}_{(\mathbf{k}+\mathbf{q})n'}}{|\mathbf{v}_{\mathbf{k}n}||\mathbf{v}_{(\mathbf{k}+\mathbf{q})n'}|}\right) \quad (4)$$

is the weight of each phonon mode in the "transport Eliashberg spectral function." Above, Ω is the unit cell volume. (The final factor dependent on the velocities above accounts for the scattering angle compared with the conventional Eliashberg spectral function [30].) Finally, the numerator in the first term of (1) is [14]

$$\frac{\bar{\sigma}_0}{\tau_{D0}} = \int_{\text{BZ}} \frac{e^2 g_s\, d\mathbf{k}}{(2\pi)^3} \sum_n \delta(\varepsilon_{\mathbf{k}n} - \varepsilon_F)(\mathbf{v}_{\mathbf{k}n} \otimes \mathbf{v}_{\mathbf{k}n}), \quad (5)$$

which is essentially the generalization of $e^2 g(\varepsilon_F)v_F^2/3$ from a spherical Fermi surface to the general anisotropic case.

We apply Monte Carlo sampling with a typical density of $\sim 10^7$ $\mathbf{k}$ values to fully converge the Brillouin zone integrals above, leveraging the Wannier interpolation of matrix elements. Plotting a histogram of the integrands in the above expressions with respect to $\epsilon_{\mathbf{k}n}$, we also evaluate the energy distributions of carriers generated upon absorption. See Ref. [28] for further details and a demonstration of the quantitative accuracy of this method for conventional plasmonic metals, as well as for low-dimensional and refractory plasmonic materials [10,31].

C. Carrier lifetimes and mean free paths

The electron-phonon contribution to the inverse lifetime is given by Fermi's golden rule as

$$\left(\tau_{\text{e-ph}}^{-1}\right)_{\mathbf{k}n} = \frac{2\pi}{\hbar} \int_{\text{BZ}} \frac{\Omega d\mathbf{k}'}{(2\pi)^3} \sum_{n'\alpha\pm} \delta(\varepsilon_{\mathbf{k}'n'} - \varepsilon_{\mathbf{k}n} \mp \hbar\omega_{\mathbf{k}'-\mathbf{k},\alpha}) \left[n_{\mathbf{k}'-\mathbf{k},\alpha} + \frac{1}{2} \mp \left(\frac{1}{2} - f_{\mathbf{k}'n'} \right) \right] |g_{\mathbf{k}'n',\mathbf{k}n}^{\mathbf{k}'-\mathbf{k},\alpha}|^2, \tag{6}$$

where the factors in order correspond to energy conservation, occupation factors, and the electron-phonon matrix elements. The sum over $\pm$ counts phonon absorption and emission processes. See Refs. [28,31] for further details.

The electron-electron contribution is calculated using

$$\left(\tau_{\text{e-e}}^{-1}\right)_{\mathbf{k}n} = \frac{2\pi}{\hbar} \int_{\text{BZ}} \frac{d\mathbf{k}'}{(2\pi)^3} \sum_{n'} (f_{\mathbf{k}'n'} + n_T(\varepsilon_{\mathbf{k}'n'} - \varepsilon_{\mathbf{k}n})) \sum_{\mathbf{GG}'} \frac{1}{\pi} \text{Im} \left[\frac{4\pi e^2}{|\mathbf{k}' - \mathbf{k} + \mathbf{G}|^2} \epsilon_{\mathbf{GG}'}^{-1}(\mathbf{k}' - \mathbf{k}, \varepsilon_{\mathbf{k}n} - \varepsilon_{\mathbf{k}'n'}) \right]$$

$$\times \tilde{\rho}_{\mathbf{k}'n',\mathbf{k}n}(\mathbf{G}) \tilde{\rho}_{\mathbf{k}'n',\mathbf{k}n}^*(\mathbf{G}'), \tag{7}$$

where $\tilde{\rho}_{\mathbf{q}'n',\mathbf{q}n}$ are density matrices in the plane-wave basis with reciprocal lattice vectors $\mathbf{G}$ and $\epsilon_{\mathbf{GG}'}^{-1}$ is the inverse dielectric matrix calculated in the random phase approximation. See Ref. [32] for a detailed introduction to this method and Ref. [28] for our specific implementation details. The only difference from Ref. [28] is the factor $f_{\mathbf{k}'n'} + n_T(\varepsilon_{\mathbf{k}'n'} - \varepsilon_{\mathbf{k}n})$, where $n_T(\hbar\omega) \equiv (\exp\frac{\hbar\omega}{k_B T} - 1)^{-1}$ is the Bose function, which generalizes the approach from $T = 0$ to the nonzero-temperature GW formalism [33,34]. In particular, this extension ensures a finite $\tau_{\text{e-e}}^{-1} \propto ((\varepsilon - \varepsilon_F)^2 + (\pi k_B T)^2)$ near the Fermi energy as expected for metals [35], while the conventional $T = 0$ formalism for $\tau_{\text{e-e}}$ diverges as $\varepsilon \to \varepsilon_F$ [28].

The net carrier lifetime is $\tau_{\mathbf{k}n}^{-1} = (\tau_{\text{e-ph}}^{-1})_{\mathbf{k}n} + (\tau_{\text{e-e}}^{-1})_{\mathbf{k}n}$. We use this to calculate the carrier linewidths $\text{Im}\,\Sigma_{\mathbf{k}n} = \hbar/(2\tau_{\mathbf{k}n})$ for the broadening of the energy conservation factors above, as well as for the mean free path $\lambda_{\mathbf{k}n} = |\mathbf{v}_{\mathbf{k}n}|\tau_{\mathbf{k}n}$. Note that as in previous theoretical studies [10,36], the carrier lifetime calculated here is the time for individual electron-phonon scattering events. This is distinct from the electron-phonon fall or decay time often reported in pump-probe spectroscopy [37–39]. The electron-phonon relaxation time reported in experiments is the time constant for energy transfer from the electronic subsystem to the phononic subsystem.

D. Interfacial injection probability

We estimate the probability of injecting carriers into semiconductors using a modified Fowler model that accounts for the electronic structure of the metal by directly employing band momenta $\mathbf{p}_{\mathbf{k}n} = m_e \mathbf{v}_{\mathbf{k}n}$ computed from DFT (and interpolated using Wannier functions) [16,17,40]. Specifically, for each electronic state in the metal, we decompose the momentum into a component along the interface-normal direction (assumed to be the preferred transport direction $\hat{\mathbf{j}}$), $p_{\mathbf{k}n}^\perp \equiv \mathbf{p}_{\mathbf{k}n} \cdot \hat{\mathbf{j}}$, and a component parallel to the interface, $p_{\mathbf{k}n}^\parallel \equiv (|\mathbf{p}_{\mathbf{k}n}|^2 - (p_{\mathbf{k}n}^\perp)^2)^{1/2}$.

The modified Fowler model matches the parallel component, requiring $p_{\text{SC}}^\parallel(\mathbf{p}_{\mathbf{k}n}) = p_{\mathbf{k}n}^\parallel$. Assuming a parabolic band structure for the semiconductor, the corresponding interface-normal component of the momentum is

$$p_{\text{SC}}^\perp(\mathbf{p}_{\mathbf{k}n}, \varepsilon_{\mathbf{k}n}) = \begin{cases} \sqrt{\Theta(2m_e^*(\varepsilon_{\mathbf{k}n} - \varepsilon_F - \phi_B^e) - (p_{\mathbf{k}n}^\parallel)^2)} & \text{for } \varepsilon_{\mathbf{k}n} > \varepsilon_F + \phi_B^e \\ \sqrt{\Theta(2m_h^*(\varepsilon_F - \phi_B^h - \varepsilon_{\mathbf{k}n}) - (p_{\mathbf{k}n}^\parallel)^2)} & \text{for } \varepsilon_{\mathbf{k}n} < \varepsilon_F - \phi_B^h \\ 0 & \text{otherwise,} \end{cases} \tag{8}$$

where $\Theta(x)$ is the Heaviside step function, m_e^* (m_h^*) and ϕ_B^e (ϕ_B^h) are the effective masses and Schottky barrier heights of electrons (holes) in the semiconductor, respectively. Note that states that are not allowed to enter the semiconductor lead to $p_{\text{SC}}^\perp = 0$.

Finally, the probability of injection in the modified Fowler model, accounting for a transmission matrix element due to momentum mismatch [15], is

$$P_{\mathbf{k}n}^{\text{inj}} = \frac{4v_{\mathbf{k}n}^\perp v_{\text{SC}}^\perp(\mathbf{v}_{\mathbf{k}n}, \varepsilon_{\mathbf{k}n})}{(v_{\mathbf{k}n}^\perp + v_{\text{SC}}^\perp(\mathbf{v}_{\mathbf{k}n}, \varepsilon_{\mathbf{k}n}))^2}. \tag{9}$$

In our analysis in Sec. III E, we report the average injection probability at each carrier energy,

$$P_{\text{inj}}(\varepsilon) = \frac{1}{g(\varepsilon)} \int_{\text{BZ}} \frac{g_s\, d\mathbf{k}}{(2\pi)^3} \sum_n \delta(\varepsilon_{\mathbf{k}n} - \varepsilon) P_{\mathbf{k}n}^{\text{inj}}, \tag{10}$$

where $g(\varepsilon)$ is the electronic density of states.

III. RESULTS AND DISCUSSION

A. Directional conductors

We recently identified several directional conductors that exhibit promise for conduction in nanoscale geometries using a high-throughput screening based on electronic structure calculations [41]. These materials fall into two broad classes, filmlike and wirelike conductors, which exhibit excellent transport in two perpendicular directions and along a single axis, respectively. To investigate the potential of directionality to additionally enhance harvesting of hot carriers far from equilibrium, we select two representative materials from each class. In particular, for the filmlike conductors, we select the delafossite oxide $PtCoO_2$ with the lowest resistivity and the well-studied MAX phase Cr_2AlC [where "MAX phase" refers to the family $M_{n+1}AX_n$ ($n = 1–3$), where M is an early transition metal, A is an A-group element, and X is carbon or nitrogen], while for the wirelike conductors,
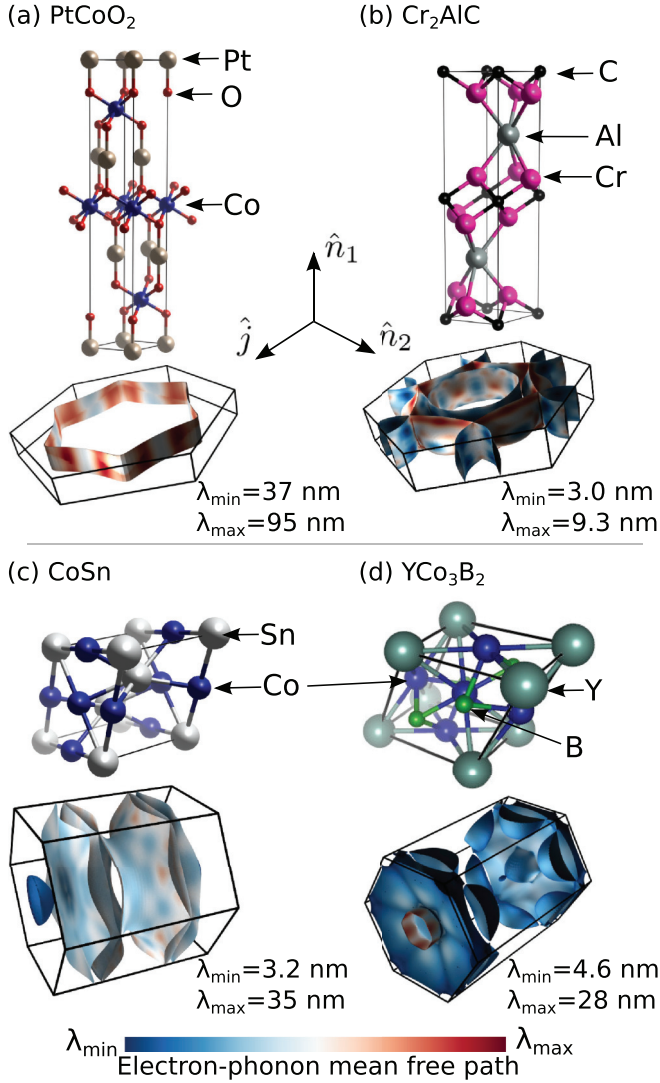
Type	Material	$\hat{\mathbf{j}}$	$\hat{\mathbf{n}}$	ρ ($\mu\Omega$ cm) Along $\hat{\mathbf{j}}$	Along $\hat{\mathbf{n}}$
Filmlike	$PtCoO_2$	$\langle 1000 \rangle$	$[0001]$	1.8	5960
	Cr_2AlC	$\langle 1000 \rangle$	$[0001]$	14.5	47.8
Wirelike	$CoSn$	$[0001]$	$\langle 1000 \rangle$	2.9	37.2
	YCo_3B_2	$[0001]$	$\langle 1000 \rangle$	5.7	37.9

Fermi surface orientations and preferred transport directions, but a much weaker anisotropy in the resistivity [44].

The remaining two materials, CoSn and YCo_3B_2, have Fermi surface sheets parallel to the hexagonal plane [Figs. 1(c) and 1(d)], leading to Fermi velocities and conduction predominantly along the c axis (Table II). These materials therefore have a single preferred transport direction, with two preferred surface-normal directions, making them suitable for conduction in nanoscale wires [41]. To discuss these filmlike and wirelike materials on a similar footing, we will henceforth refer to properties along preferred transport direction $\hat{\mathbf{j}}$ and along the preferred normal direction $\hat{\mathbf{n}}$, but note that the crystallographic orientation of these directions is different for the two classes of materials as specified in Table II.

Finally, note that the $\hat{\mathbf{j}}$ resistivity for all these conductors, except for the Cr_2AlC MAX phase, is comparable to that for the most common plasmonic metals (1.6, 1.7, 2.3, and 2.8 $\mu\Omega$ cm for silver, copper, gold, and aluminium [28]), while the $\hat{\mathbf{n}}$ resistivity is much larger. This difference for Cr_2AlC can be understood by comparing the electronic structures of the four materials (see Fig. S1 in the Supplemental Material [26]). In Cr_2AlC, the states near the Fermi level are dominated by d bands [45], which tend to be narrower and hence have smaller velocities and larger density of states at the Fermi level. The other three materials studied here ($PtCoO_2$, YCo_3B_2, and CoSn) have larger Fermi velocities and smaller densities of states due to larger dispersion of the bands crossing the Fermi level. Consequently, Cr_2AlC exhibits higher electron-phonon scattering rates with more states to scatter into, leading to overall worse transport properties including bulk resistivity, carrier lifetimes, and mean free paths.

FIG. 1. Unit cell structure and Fermi surfaces of the directional conductors studied here. Note that all are 3D hexagonal crystals, but have Fermi velocities (Fermi surface normals) along the a directions for the filmlike conductors [(a) and (b)] and along the c direction for the wirelike conductors [(c) and (d)]. The electron-phonon mean free path λ varies substantially over the Fermi surface for all four materials.

B. Optical response

To investigate the suitability of these materials for plasmonic applications, we first consider their Drude response. Figure 2 shows the calculated transport Eliashberg spectral functions (Sec. II B) and corresponding frequency-dependent Drude momentum relaxation times due to electron-phonon scattering. The electron-phonon coupling at the Fermi level is weakest for $PtCoO_2$, as indicated by the lowest spectral function magnitude in Fig. 2(a), followed by CoSn, YCo_3B_2, and, finally, Cr_2AlC. Correspondingly, the Drude relaxation time τ_D at low frequencies drops from $\sim$60 fs for $PtCoO_2$ to $\sim$18 fs for YCo_3B_2, in the same order.

we select the two most conductive materials, CoSn and YCo_3B_2.

Figure 1 shows the unit cell structure and Fermi surfaces for all four materials. $PtCoO_2$ exhibits an almost perfect hexagonal-prism-shaped Fermi surface, which leads to all the Fermi velocities being directed in the hexagonal plane of the material [42]. This leads to an in-plane resistivity, along the preferred transport direction $\hat{\mathbf{j}}$, that is $\sim$3000 times smaller than the out-of-plane resistivity along the preferred surface-normal direction $\hat{\mathbf{n}}$ (Table II). Such large anisotropies have been reported for transport properties of two-dimensional materials such as graphene [43], attributed to the weak van der Waals coupling between layers. However, all of the directional materials we investigate here are 3D crystals with strong bonding in all directions (Fig. 1). Cr_2AlC also has similar
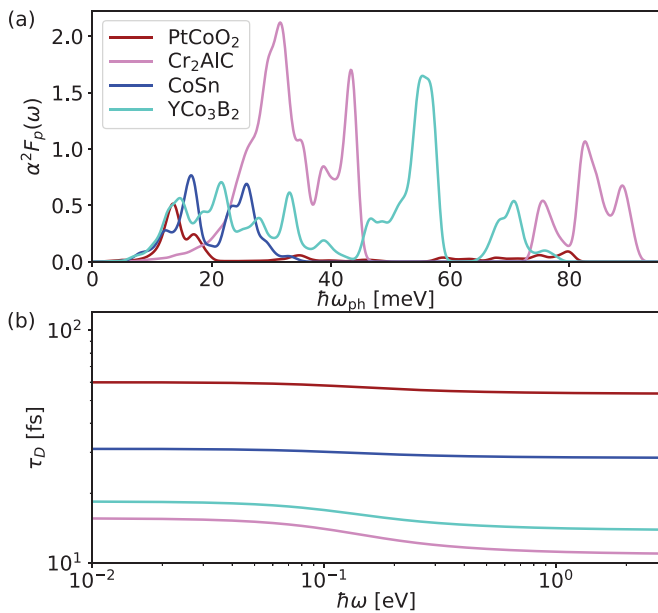
FIG. 2. (a) Transport-weighted Eliashberg spectral function and (b) frequency-dependent Drude relaxation time for directional conductors. $PtCoO_2$ exhibits the lowest electron-phonon coupling strength [lowest $\alpha^2 F(\omega)$] and hence the highest relaxation time τ_D, while Cr_2AlC has the strongest coupling and lowest τ_D. The relaxation time drops from the $\omega = 0$ value for $\omega \sim \omega_{ph}$ and saturates to a high-frequency limit for $\omega \gg \omega_{ph}$ for each material.

With increasing frequency, Drude relaxation can access higher-energy phonon modes that were inaccessible using thermal energy at room temperature alone, causing τ_D to decrease. For $PtCoO_2$, τ_D decreases from 60 fs at low frequency to ~54 fs at optical frequencies, remaining larger than the low-frequency relaxation time for most elemental metals! The largest proportional drop in τ_D is from 15.6 to 11 fs for Cr_2AlC, which has the highest-energy phonon spectrum, while the smallest drop in τ_D is from 31 to 28 fs for CoSn with the lowest-energy phonon spectrum.

The decrease in τ_D with frequency accounts for phonon-assisted transitions along with the Drude term [14], which we then combine with predictions of direct transitions (Sec. II B) to compute the overall complex dielectric functions shown in Fig. 3. Note that the dielectric functions are highly anisotropic, with qualitative differences between the $\hat{\mathbf{j}}$ and $\hat{\mathbf{n}}$ directions for these directional conductors. In particular, the plasmonic window—the region with Re $\epsilon < 0$—is much larger along the $\hat{\mathbf{j}}$ direction than along the $\hat{\mathbf{n}}$ direction. The plasmonic windows of $PtCoO_2$, CoSn, and YCo_3B_2 each extend above 2.5 eV along $\hat{\mathbf{j}}$, surpassing the plasmonic range of gold (2.6 eV) and approaching that of silver (3.4 eV) [35]. In contrast, the plasmonic window along $\hat{\mathbf{n}}$ is below 0.5 eV for all four materials, with that of $PtCoO_2$ (the most anisotropic of the four) being virtually negligible.

Additionally, Im ϵ along the preferred transport directions are relatively low when Re ϵ crosses zero, indicating a plasmonic response with quality factors comparable to noble metals, most notably for CoSn. In the plasmonic frequency range for $\hat{\mathbf{j}}$, most of these materials exhibit dielectriclike behavior, Re $\epsilon \gg$ Im $\epsilon > 0$, along the $\hat{\mathbf{n}}$ direction. Consequently,
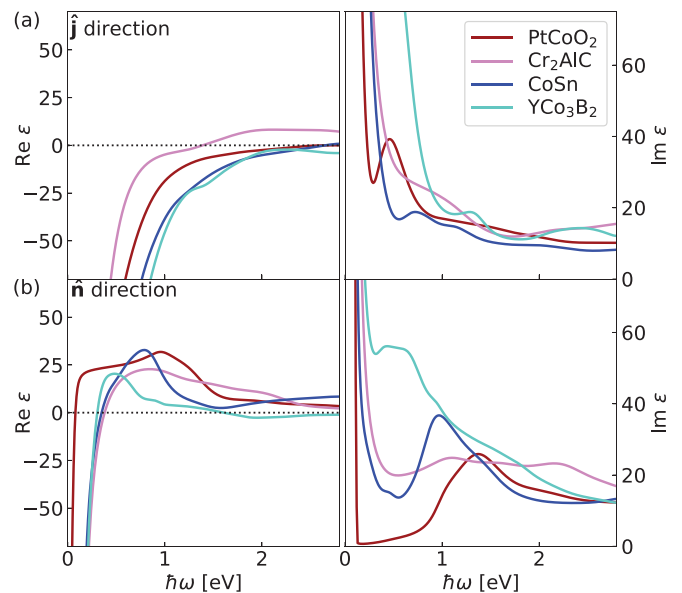

FIG. 3. Complex dielectric function for the directional conductors along (a) the preferred transport direction $\hat{\mathbf{j}}$ and (b) the corresponding normal direction $\hat{\mathbf{n}}$, with real and imaginary parts in the left and right columns, respectively. The plasmonic window (Re $\epsilon < 0$) is much wider along the $\hat{\mathbf{j}}$ direction than along the $\hat{\mathbf{n}}$ direction in all cases, making the optical response of the film conductors $PtCoO_2$ and Cr_2AlC similar to 2D materials and that of wire conductors CoSn and YCo_3B_2 similar to that of 1D materials, even though all four materials are 3D materials with strong bonding in all directions.

these materials essentially behave like lower-dimensional materials optically: The filmlike conductors behave like 2D materials and the wirelike conductors behave like 1D materials, but we emphasize again that these materials are 3D crystals bonded strongly in all directions. This opens up the possibility of reaping the advantages of low-dimensional plasmonics, such as high confinement [14], while working with easier-to-process 3D materials. See the Supplemental Material for tables of predicted dielectric functions to facilitate the design of plasmonic structures using these materials [26]; we focus here instead on material properties including hot carrier distributions and transport next.

C. Hot carrier generation

Plasmon decay is captured by the imaginary part of the dielectric functions, Im $\epsilon(\omega)$, and the energy $\hbar\omega$ lost by the plasmon is deposited in an electron-hole pair. Figure 4 shows the energy distribution of hot carriers excited upon plasmon decay, calculated by resolving contributions to Im $\epsilon(\omega)$ by carrier energy ε (Sec. II B) [28]. Unlike a clear separation between phonon-assisted transitions below an interband threshold and direct transition above it in typical plasmonic metals [10,28], these complex conductors exhibit direct transitions at almost all plasmon frequencies. Only $PtCoO_2$ and CoSn show a small frequency range ($\hbar\omega < 0.5$ eV) where indirect phonon-assisted transitions contribute significantly. Interestingly, the relative importance of phonon-assisted transitions in $PtCoO_2$ is enhanced along the $\hat{\mathbf{n}}$ direction, indicating
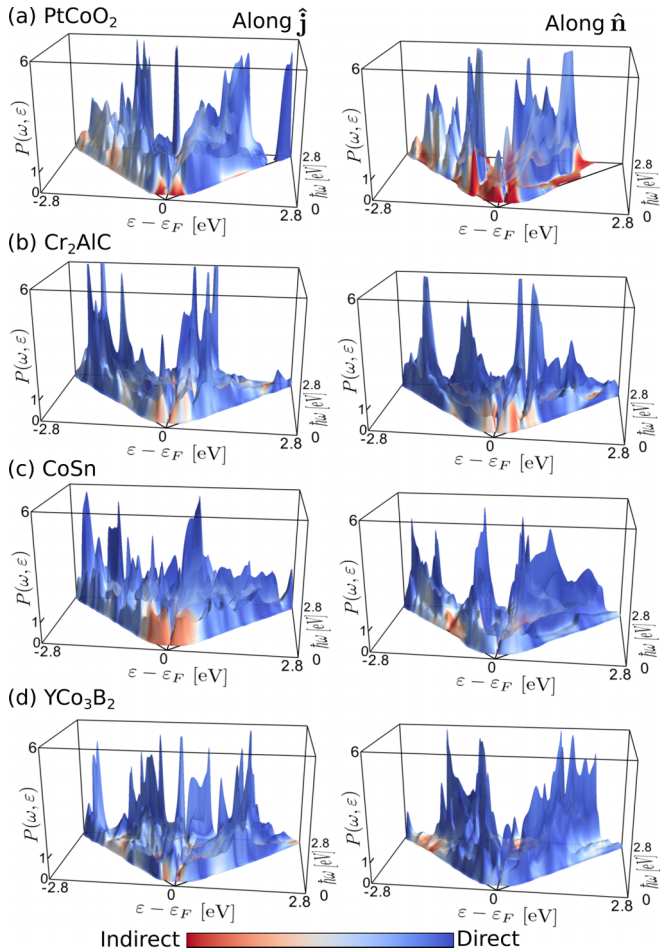
FIG. 4. (a)–(d) Hot carrier distribution, $P(\omega, \varepsilon)$, as a function of carrier energy ε and plasmon frequency ω for directional conductors, with plasmon electric field polarized along their corresponding $\hat{\mathbf{j}}$ directions (left panels) and $\hat{\mathbf{n}}$ directions (right panels). The probability is normalized such that $P(\omega, \varepsilon) = 1$ for a uniform electron and hole energy distribution [28]. Note that direct transitions dominate at almost all plasmon frequencies, except for $\hbar\omega \ll 1$ eV in PtCoO$_2$ and CoSn, leading to carrier distributions that are sensitive to electronic structure details.
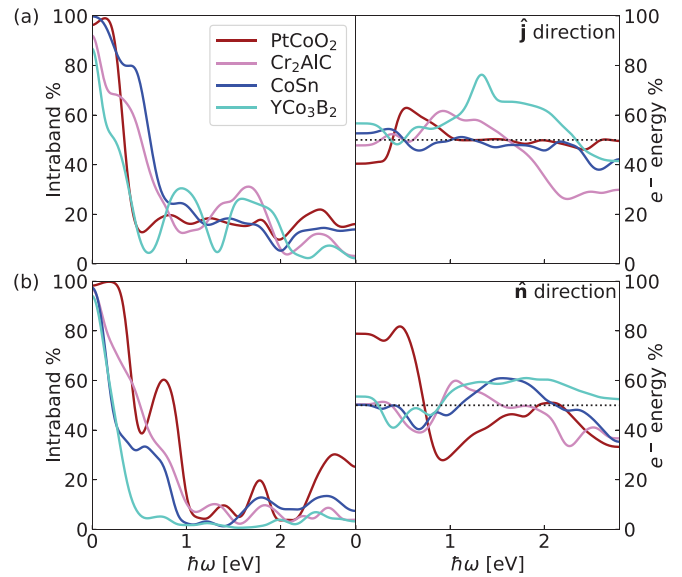

FIG. 5. Fraction of interband absorption (left column) and fraction of energy in hot electrons (right column) for the directional conductors for light polarized along (a) the preferred transport direction $\hat{\mathbf{j}}$ and (b) the corresponding normal direction $\hat{\mathbf{n}}$. Interband absorption is stronger along the $\hat{\mathbf{j}}$ direction but is dominated by direct absorption for photons with energy larger than 1 eV in all cases. Energy is evenly distributed between electrons and holes, except for low-energy intraband-dominated absorption of $\hat{\mathbf{n}}$-polarized light in PtCoO$_2$.

a selection rule that the lowest-energy direct transitions are allowed only for in-plane electric fields in this material.

The predominance of direct transitions leads to relatively complex energy distributions of carriers, sensitive to details in the electronic structure. Consequently, Fig. 5 shows moments of these carrier distributions, indicating the fraction of (indirect) intraband transitions and the distribution of energy between electrons and holes. Direct transitions dominate above 1 eV, with the intraband fraction dropping below 20%, in all four materials. Additionally, despite the complex and different structure in the electron and hole distributions in Fig. 4, the overall energy separation between electrons and holes is approximately even, with between 40 and 60% of the energy in the electrons, across the frequency range considered for all materials. The only notable deviation is that 80% of the energy is deposited in the electrons by intraband transitions in PtCoO$_2$ for $\hat{\mathbf{n}}$ polarization, while the energy split is close to equal even in that energy range for the $\hat{\mathbf{j}}$ polarization. Overall,

given the absence of systematic asymmetries in electron and hole distributions, like those that exist for noble metals [28], analyses of hot carriers in these directional conductors may safely assume a uniform electron and hole energy distribution extending from 0 to the plasmon energy, independent of polarization.

Note that the hot carrier properties presented here are calculated for bulk materials. Since surface sites (such as edges, facets, and corners) and the shape and size of the nanoparticles can significantly enhance the rate and distribution of hot carrier generation [46], future studies should focus on the effect of atomic structure on plasmonic properties of these directional conductors. Additionally, nanoparticle shapes and surface characteristics will vary dramatically depending on the synthesis approach and present additional opportunities in targeting techniques such as self-organized nanodecomposition [47] towards nanoparticles suitable for hot carrier extraction in future work.

D. Carrier transport

Efficient hot carrier harvesting requires extraction of the carriers from the metal prior to thermalization by electron-phonon and electron-electron scattering. Figures 6 and 7 show the predicted lifetime and mean free path of hot carriers in the directional conductors, respectively, accounting for both these scattering mechanisms (Sec. II C). Electron-phonon scattering dominates near the Fermi energy, while the phase space for electron-electron scattering increases with increasing electron or hole energies and eventually dominates over electron-phonon scattering, exactly analogous to the case
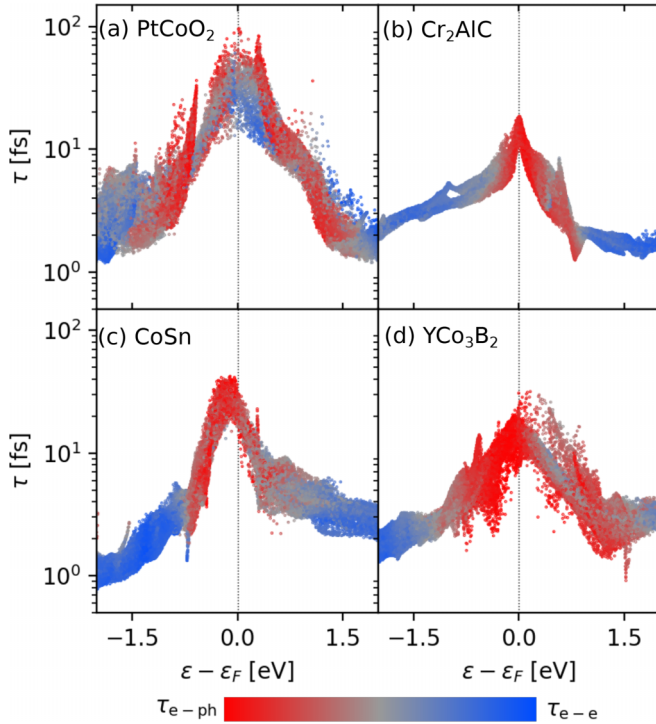
FIG. 6. (a)–(d) Lifetime of hot carriers as a function of carrier energy in directional conductors, with color indicating relative contributions of electron-phonon and electron-electron scattering. Carrier lifetimes are comparable in magnitude to noble metals, especially in $PtCoO_2$ and CoSn, but drop off with energy faster than for noble metals [28].
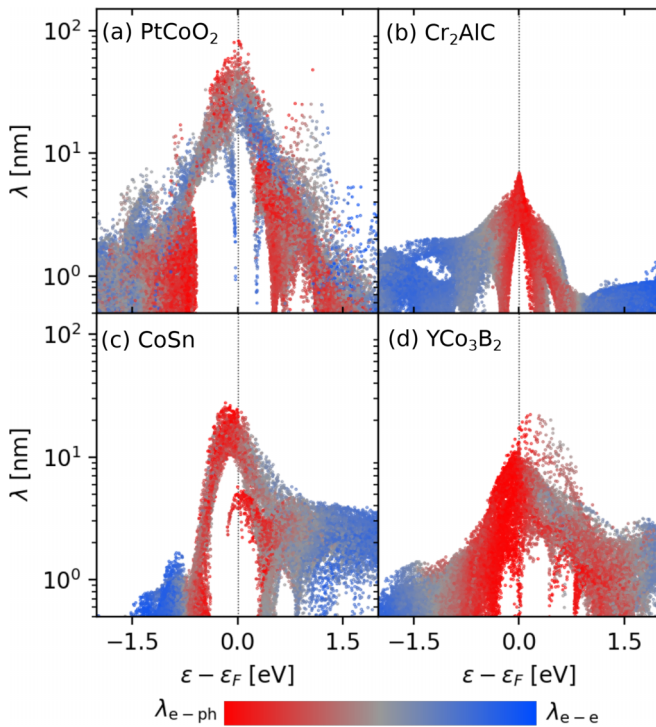

FIG. 7. (a)–(d) Mean free path of hot carriers as a function of carrier energy in directional conductors, with behavior closely following those of the lifetimes shown in Fig. 6.

for other plasmonic metals including elemental metals and transition metal nitrides [10,28]. The mean free paths drop off with energy more quickly than the lifetimes in most of the materials, especially for the holes, indicating a reduction in average carrier velocities for energies far from the Fermi level.

The peak carrier lifetimes and mean free paths in these materials are competitive with noble metals, especially in $PtCoO_2$ and CoSn. However, the drop-off with energy is faster in these materials compared with noble metals, with mean free paths dropping below 10 nm for carriers with 1 eV energies for all four materials. This is partly because the directionality of the electronic structure is a feature restricted to a narrow energy window surrounding the Fermi energy, with a marked increase in density of states away from the Fermi energy (Fig. S1 in the Supplemental Material [26]), leading to a corresponding increase in the phase space for scattering for higher-energy carriers. This indicates the need to carefully design plasmonic geometries to minimize the average distance between the location of carrier generation and the interfaces where carriers can be collected to below 10 nm.

E. Carrier injection across interfaces

The final step in hot carrier harvesting is transferring the carriers across an interface, such as a metal-semiconductor interface, prior to energy relaxation in the metal. This step is typically the largest limiting factor in hot carrier collection efficiency because most carriers in the metal encounter total internal reflection at the interface with the semiconductor, as captured by the semiclassical Fowler model of carrier injection [6,15]. In particular, the injection from noble metals into semiconductors at energies just above the Schottky barriers is typically ~0.1% or smaller due to the large mismatch between the Fermi velocity in the metal and velocities near the band edges of the semiconductor [16]. Injection from lower-velocity bands of the metal, such as d bands in copper, can slightly increase these probabilities, but they remain at that small order of magnitude [17].

The directional conductors investigated here have the potential to remedy this issue in two ways. First, the Fermi velocity in these materials is lower than in noble metals, exhibiting a slightly better match to velocities near semiconductor band edges. Second, the directionality of the velocity makes it possible to substantially reduce the component parallel to the surface (that needs to match across the interface) by collecting in an interface whose normal is along $\hat{\mathbf{j}}$.

Figure 8(a) shows that the component of carrier velocity direction $\hat{\mathbf{v}}$ along $\hat{\mathbf{j}}$ is close to 1 for wirelike conductors CoSn and YCo_3B_2, indicating that the remaining components must be much smaller. This projection is smaller for the filmlike conductors, which have large velocity components along two orthogonal directions, and approaches the isotropic limit of $1/2$ for a noble metal such as gold. Figures 8(b) and 8(c) show that this directionality of the velocity indeed leads to a significantly larger injection probability than for the case of gold, as predicted using a modified Fowler model (Sec. II D). Compared with $P_{inj} \sim 10^{-3}$ in gold, all directional conductors have the potential to inject with >10%

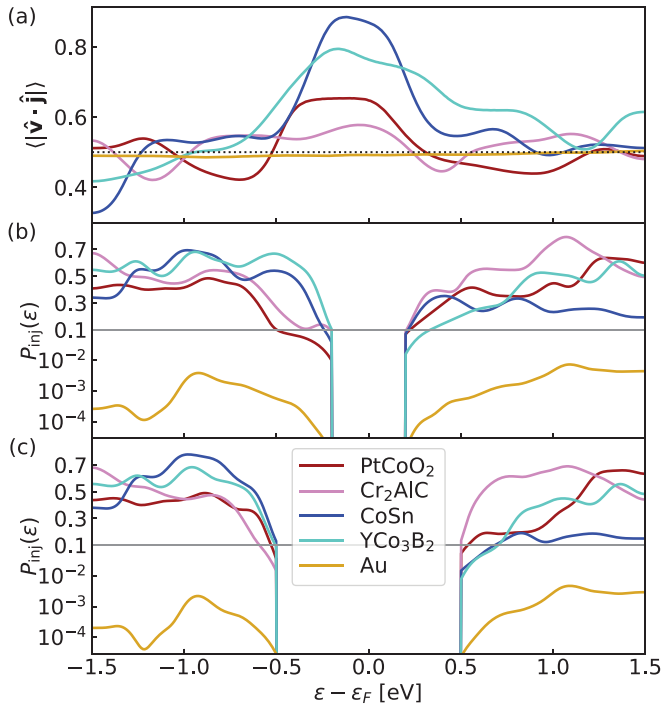FIG. 8. (a) Average velocity direction $\hat{\mathbf{v}}$ component along preferred transport direction $\hat{\mathbf{j}}$ in directional conductors compared with gold, as a function of carrier energy. (The dotted line at $\langle|\hat{\mathbf{v}} \cdot \hat{\mathbf{j}}|\rangle = 1/2$ indicates the isotropic limit.) The preferred orientation of velocities substantially increases the probability of carrier injection into a semiconductor (assumed parabolic bands with $m^* = 0.3 m_e$) with Schottky barrier heights (b) 0.2 eV and (c) 0.5 eV. Note the switch from logarithmic to linear scaling in the y axis of (b) and (c) to simultaneously show the small injection probabilities from gold and the much larger injection probabilities from all directional conductors.

probability into a model semiconductor (assuming a typical electron and hole mass of 0.3 for simplicity), presenting significant opportunities for efficient plasmonic hot carrier harvesting.

IV. CONCLUSIONS

Using first-principles calculations of optical response, carrier generation, transport, and injection, we show the significant promise of directional conductors for plasmonic hot carrier applications. The strong anisotropy of the Fermi velocity in these materials to one or two directions introduces 1D wirelike or 2D filmlike behavior in a 3D-crystalline material. These materials exhibit a plasmonic response over a range of frequencies comparable to noble metals along the preferred transport direction(s) $\hat{\mathbf{j}}$, while simultaneously exhibiting dielectric behavior in the preferred normal direction(s) $\hat{\mathbf{n}}$ at those frequencies, mimicking the optical response of a lower-dimensional metal. Hot carrier generation and transport are also similar to noble metals, but directionality in the momenta shows promise for orders-of-magnitude-higher efficiency in extraction of hot carriers from these materials into semiconductors. The dielectric functions, carrier transport, and injection models reported here can now be used to design plasmonic nanostructures with the potential for high-efficiency hot carrier harvesting.

[1] S. Linic, P. Christopher, and D. B. Ingram, Nat. Mater. **10**, 911 (2011).

[2] P. J. Schuck, Nat. Nanotechnol. **8**, 799 (2013).

[3] F. Wang and N. A. Melosh, Nano Lett. **11**, 5426 (2011).

[4] M. Moskovits, Nat. Nanotechnol. **10**, 6 (2015).

[5] M. L. Brongersma, N. J. Halas, and P. Nordlander, Nat. Nanotechnol. **10**, 25 (2015).

[6] S. Kumar, A. Habib, and R. Sundararaman, Trends Chem. **3**, 902 (2021).

[7] U. Guler, A. Boltasseva, and V. M. Shalaev, Science **344**, 263 (2014).

[8] P. Patsalas, N. Kalfagiannis, S. Kassavetis, G. Abadias, D. V. Bellas, C. Lekka, and E. Lidorikis, Mater. Sci. Eng. R Rep. **123**, 1 (2018).

[9] S. Ishii, S. L. Shinde, W. Jevasuwan, N. Fukata, and T. Nagao, ACS Photonics **3**, 1552 (2016).

[10] A. Habib, F. Florio, and R. Sundararaman, J. Opt. **20**, 064001 (2018).

[11] K. Hantanasirisakul and Y. Gogotsi, Adv. Mater. **30**, 1804779 (2018).

[12] D. B. Velusamy, J. K. El-Demellawi, A. M. El-Zohry, A. Giugni, S. Lopatin, M. N. Hedhili, A. E. Mansour, E. D.

Fabrizio, O. F. Mohammed, and H. N. Alshareef, Adv. Mater. **31**, 1807658 (2019).

[13] J. Jeon, H. Choi, S. Choi, J.-H. Park, B. H. Lee, E. Hwang, and S. Lee, Adv. Funct. Mater. **29**, 1905384 (2019).

[14] R. Sundararaman, T. Christensen, Y. Ping, N. Rivera, J. D. Joannopoulos, M. Soljačić, and P. Narang, Phys. Rev. Mater. **4**, 074011 (2020).

[15] H. Chalabi, D. Schoen, and M. L. Brongersma, Nano Lett. **14**, 1374 (2014).

[16] G. Tagliabue, A. Jermyn, R. Sundararaman, A. Welch, J. DuChene, R. Pala, A. Davoyan, P. Narang, and H. Atwater, Nat. Commun. **9**, 3394 (2018).

[17] G. Tagliabue, J. S. DuChene, A. Habib, R. Sundararaman, and H. A. Atwater, ACS Nano **14**, 5788 (2020).

[18] R. Sundararaman, K. Letchworth-Weaver, K. Schwarz, D. Gunceler, Y. Ozhabes, and T. A. Arias, SoftwareX **6**, 278 (2017).

[19] J. P. Perdew, K. Burke, and M. Ernzerhof, Phys. Rev. Lett. **77**, 3865 (1996).

[20] K. F. Garrity, J. W. Bennett, K. M. Rabe, and D. Vanderbilt, Comput. Mater. Sci. **81**, 446 (2014).

[21] P. Kushwaha, V. Sunko, P. J. Moll, L. Bawden, J. M. Riley, N. Nandi, H. Rosner, M. P. Schmidt, F. Arnold, E. Hassinger, T. K. Kim, M. Hoesch, A. P. Mackenzie, and P. D. C. King, Sci. Adv. **1**, e1500692 (2015).

[22] Z. Lin, Y. Zhou, M. Li, and J. Wang, Int. J. Mater. Res. **96**, 291 (2005).

[23] W. R. Meier, M.-H. Du, S. Okamoto, N. Mohanta, A. F. May, M. A. McGuire, C. A. Bridges, G. D. Samolyuk, and B. C. Sales, Phys. Rev. B **102**, 075148 (2020).

[24] A. Kowalczyk, Phys. Status Solidi B **218**, 495 (2000).

[25] I. Souza, N. Marzari, and D. Vanderbilt, Phys. Rev. B **65**, 035109 (2001).

[26] See Supplemental Material at http://link.aps.org/supplemental/10.1103/PhysRevMaterials.6.125201 for electron and phonon band structures, supercell convergence of real-space representations of matrix elements, tables of predicted dielectric functions, spectral functions, and injection probabilities.

[27] S. Poncé, F. Macheda, E. R. Margine, N. Marzari, N. Bonini, and F. Giustino, Phys. Rev. Res. **3**, 043022 (2021).

[28] A. M. Brown, R. Sundararaman, P. Narang, W. A. Goddard, and H. A. Atwater, ACS Nano **10**, 957 (2016).

[29] R. Sundararaman, P. Narang, A. S. Jermyn, W. A. Goddard III, and H. A. Atwater, Nat. Commun. **5**, 5788 (2014).

[30] P. B. Allen, Phys. Rev. B **3**, 305 (1971).

[31] P. Narang, L. Zhao, S. Claybrook, and R. Sundararaman, Adv. Opt. Mater. **5**, 1600914 (2017).

[32] F. Ladstädter, U. Hohenester, P. Puschnig, and C. Ambrosch-Draxl, Phys. Rev. B **70**, 235125 (2004).

[33] L. X. Benedict, C. D. Spataru, and S. G. Louie, Phys. Rev. B **66**, 085116 (2002).

[34] J. J. Kas and J. J. Rehr, Phys. Rev. Lett. **119**, 176403 (2017).

[35] A. M. Brown, R. Sundararaman, P. Narang, W. A. Goddard III, and H. A. Atwater, Phys. Rev. B **94**, 075120 (2016).

[36] A. M. Brown, R. Sundararaman, P. Narang, A. M. Schwartzberg, W. A. Goddard III, and H. A. Atwater, Phys. Rev. Lett. **118**, 087401 (2017).

[37] M.-N. Su, C. J. Ciccarino, S. Kumar, P. D. Dongare, S. A. Hosseini Jebeli, D. Renard, Y. Zhang, B. Ostovar, W.-S. Chang, P. Nordlander, N. J. Halas, R. Sundararaman, P. Narang, and S. Link, Nano Lett. **19**, 3091 (2019).

[38] J. A. Tomko, S. Kumar, R. Sundararaman, and P. E. Hopkins, J. Appl. Phys. **129**, 193104 (2021).

[39] Y. Hattori, J. Meng, K. Zheng, A. Meier de Andrade, J. Kullgren, P. Broqvist, P. Nordlander, and J. Sá, Nano Lett. **21**, 1083 (2021).

[40] G. Tagliabue, J. S. DuChene, M. Abdellah, A. Habib, D. J. Gosztola, Y. Hattori, W.-H. Cheng, K. Zheng, S. E. Canton, R. Sundararaman, J. Sá, and H. A. Atwater, Nat. Mater. **19**, 1312 (2020).

[41] S. Kumar, C. Multunas, B. Defay, D. Gall, and R. Sundararaman, Phys. Rev. Mater. **6**, 085002 (2022).

[42] V. Eyert, R. Frésard, and A. Maignan, Chem. Mater. **20**, 2370 (2008).

[43] E. Pop, V. Varshney, and A. K. Roy, MRS Bull. **37**, 1273 (2012).

[44] M. Bugnet, M. Jaouen, V. Mauchamp, T. Cabioc'h, and G. Hug, Phys. Rev. B **90**, 195116 (2014).

[45] T. Ito, D. Pinek, T. Fujita, M. Nakatake, S.-i. Ideta, K. Tanaka, and T. Ouisse, Phys. Rev. B **96**, 195168 (2017).

[46] T. P. Rossi, P. Erhart, and M. Kuisma, ACS Nano **14**, 9963 (2020).

[47] T. Dietl, K. Sato, T. Fukushima, A. Bonanni, M. Jamet, A. Barski, S. Kuroda, M. Tanaka, P. N. Hai, and H. Katayama-Yoshida, Rev. Mod. Phys. **87**, 1311 (2015).